SATELLITE AND IN SITU SALINITY

Understanding Near-Surface Stratification and Subfootprint Variability

BY J. Boutin, Y. Chao, W. E. Asher, T. Delcroix, R. Drucker, K. Drushka, N. Kolodziejczyk, T. Lee, N. Reul, G. Reverdin, J. Schanze, A. Soloviev, L. Yu, J. Anderson, L. Brucker, E. Dinnat, A. Santos-Garcia, W. L. Jones, C. Maes, T. Meissner, W. Tang, N. Vinogradova, and B. Ward

A synthesis of present knowledge about the formation and evolution of vertical and horizontal variability in near-surface salinity at scales relevant to satellite salinity is presented.

L-band microwave radiometers on both the Soil Moisture Ocean Salinity (SMOS; Mecklenburg et al. 2012) and Aquarius/Satélite de Aplicaciones Científicas-D (SAC-D) (Lagerloef 2012) satellites have now demonstrated that they are capable of measuring sea surface salinity (SSS). They provide near-global coverage, a spatial resolution ranging from 43 to 150 km, and a precision useful for detailed oceanographic studies, that is, ±0.2 practical salinity scale (pss) [salinity is a dimensionless quantity and will be reported on the Practical Salinity Scale of 1978 (PSS-78; IOC et al. 2010, and references therein) in the rest of the text] on monthly time scales and 100×100 km^2 spatial scales (Drucker and Riser 2014; Hernandez et al. 2014; Hasson et al. 2013). This new capability provides an unprecedented global view of surface salinity, a key state variable that determines ocean circulation and is tied to the global water cycle (Reul et al. 2014c). These satellite-derived salinity data provide new insight into the spatial and temporal variability of SSS (Alory et al. 2012; Busecke et al. 2014; Hasson et al. 2014; Kolodziejczyk et al. 2015; Lee et al. 2014; Menezes et al. 2014; Qu et al. 2014; Reul et al. 2014a).

Photo: Raindrops on a water surface. [ID 5563454 ©Sailorman: Dreamstime.com.]

The success of satellite salinity measurements suggests new possibilities of using global maps of salinity to monitor and understand ocean dynamics and the global hydrological cycle. However, calibration and validation of satellite-retrieved salinity is an ongoing process that requires comparison of satellite SSS values with spatially and temporally collocated in situ values. There are two key differences between

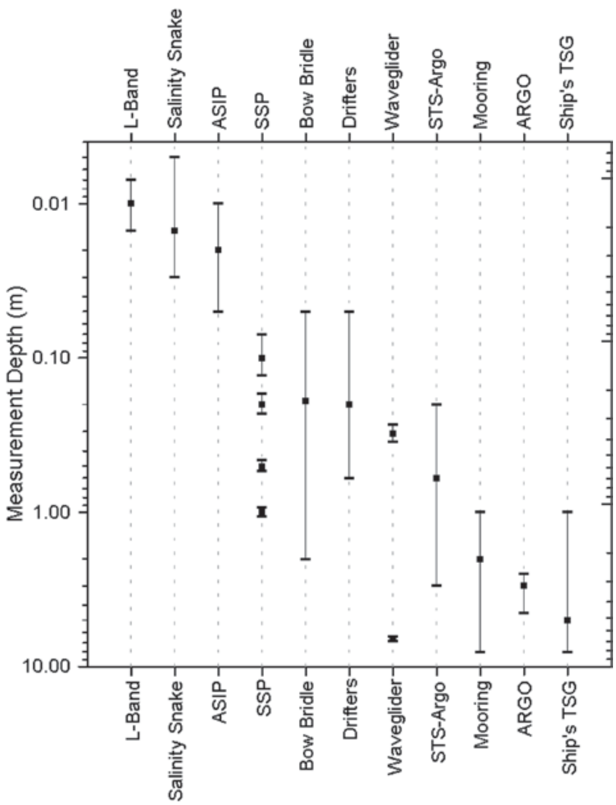

Fig. 1. Scale portraying the typical depth at which near-surface salinity is measured by various sensors/platforms. The small squares show the average measurement depth and the capped lines show the range for that average. For profiling platforms (ASIP, Bow Bridle, STS–Argo, and Argo) the range represents the variability of the topmost point in the profile. For platforms with standardized configurations that measure at fixed depths (Salinity Snake, Surface Salinity Profiler (SSP), and Wave Glider) the mean and range of each sensor at a particular depth are shown. For platforms where there are multiple sensor configurations (drifters, mooring, and shipborne TSG) or that sample at different depths depending on the specifics of the platform, the range of measurement depths across all platforms is shown. Radiometric penetration depths were calculated as in Anguelova and Gaiser (2011) and show penetration depths at 1.43 GHz over the salinity range of 20–38 pss and temperature range of –2° to 35°C (where the "mean" value shown in the figure is for 20°C and 35 pss). Details for each platform can be found as follows: Salinity Snake, Schanze et al. (2014); ASIP, Ward et al. (2014); SSP, Asher et al. (2014a); Bow Bridle, Soloviev and Lukas (1996); Drifters, Reverdin et al. (2012, 2013) and Centurioni et al. (2015); Wave Glider, Hodges and Fratantoni (2014); STS–Argo/Argo, Anderson and Riser (2014); Mooring, McPhaden et al. (1998, 2010), Bourlès et al. (2008), and Farrar et al. (2015); and the ship's TSG, W. E. Asher (2015, personal communication, online survey of TSG intake depths).

AFFILIATIONS: Boutin, Kolodziejczyk,* and Reverdin—LOCEAN Laboratory, Sorbonne Universités (University Pierre and Marie Curie, University of Paris 6)-CNRS-IRD-MNHN, Paris, France; Chao—Remote Sensing Solutions, Pasadena, California; Asher and Drushka—Applied Physics Laboratory, University of Washington, Seattle, Washington; Delcroix—Laboratoire d'Etudes en Géophysique et Océanographie Spatiale, Toulouse, France; Drucker and Anderson—School of Oceanography, University of Washington, Seattle, Washington; Lee and Tang—Jet Propulsion Laboratory, Pasadena, California; Reul—Laboratory of Oceanography from Space, IFREMER, Toulon, France; Schanze—Earth and Space Research, Seattle, Washington; Soloviev—Nova Southeastern University, Dania Beach, Florida; Yu—Woods Hole Oceanographic Institution, Woods Hole, Massachusetts; Brucker—Universities Space Research Association, and National Aeronautics and Space Administration Goddard Space Flight Center, Greenbelt, Maryland; Dinnat—Cryospheric Sciences Laboratory, National Aeronautics and Space Administration Goddard Space Flight Center, Greenbelt, Maryland, and Center of Excellence in Earth Systems Modeling and Observations, Chapman University, Orange, California; Garcia and Jones—Electrical and Computer Engineering Department, University of Central Florida, Orlando, Florida; Maes—Laboratoire de Physique des Océans, CNRS-Ifremer-IRD-UBO, Plouzané, France; Meissner—Remote Sensing Systems, Santa Rosa, California; Vinogradova—Atmospheric and Environmental Research, Lexington, Massachusetts; Ward—AirSea Laboratory, School of Physics, and Ryan Institute, National University of Ireland, Galway, Galway, Ireland
***CURRENT AFFILIATION:** Kolodziejczyk—Laboratoire de Physique des Océan (CNRS-IRD-UBO-Ifremer), Plouzané, France
CORRESPONDING AUTHOR: Jacqueline Boutin, Senior Researcher, LOCEAN Laboratory, 4 place Jussieu, F-75005 Paris, France
E-mail: jb@locean-ipsl.upmc.fr

The abstract for this article can be found in this issue, following the table of contents.
DOI:10.1175/BAMS-D-15-00032.1

In final form 19 November 2015

satellite and in situ salinity. First, because of the short penetration depth of microwave radiation into the ocean (Swift 1980), microwave radiometers measure salinity in the top few centimeters of the ocean. In contrast, in situ measurements commonly used for calibration and validation (e.g., Argo floats, moorings, and ship observations) are made at depths of a few meters (Fig. 1). Second, a satellite measures salinity as a spatial average over the satellite's footprint, whereas in situ sensors provide data at a single point [SMOS synthetic antennas have variable elliptical footprints over the field of view of 43-km resolution on average (Kerr et al. 2010), while the three beams for Aquarius are approximately elliptical and have footprints of 76 × 94, 84 × 120, and 96 × 156 km^2 (Lagerloef 2012)]. Therefore, if the ocean salinity field contains vertical gradients in the upper few meters, or if the ocean surface salinity has significant horizontal or temporal variability, there could be a physical difference between the satellite and in situ salinity values that would complicate calibration and validation of the satellite's performance. The target defined for these satellite missions is to achieve a precision of 0.1–0.2 pss. This precision is sufficient to detect typical interannual SSS variability, such as that linked to El Niño–Southern Oscillation or to the Indian Ocean dipole, seasonal SSS variability in areas that have significant seasonal cycles [shown by Bingham et al. (2012) to cover 37% of the ocean surface between 60°N and 60°S and have a median seasonal SSS amplitude of 0.19 pss], mesoscale transport of salt by large eddies across strong fronts (Reul et al. 2014a; Kolodziejczyk et al. 2015), or intraseasonal SSS variability (Li et al. 2015, and references therein).

This paper synthesizes present knowledge of the processes that contribute to the formation and evolution of near-surface vertical salinity gradients and subfootprint-scale variability. The magnitude of these gradients is quantified whenever possible as a function of environmental conditions. The potential impact of both vertical salinity gradients and subfootprint-scale variability on satellite and in situ salinity data comparisons will be discussed.

VERTICAL STRATIFICATION AND SUBFOOTPRINT VARIATIONS. Vertical stratification in the density of the upper ocean is controlled by the vertical profiles of temperature and salinity. Vertical stratification in temperature has been extensively studied over the past several decades, as it is responsible for observed differences in sea surface temperatures derived from infrared radiometers, microwave radiometers, and in situ measurements (Minnett and Kaiser-Weiss 2012, and references therein). In contrast, relatively few studies of upper-ocean salinity stratification [see the recent climatology discussed by Maes and O'Kane (2014)] have been performed. The addition of freshwater to the ocean surface (from precipitation, river runoff, or melting of sea ice) and the removal of freshwater (through evaporation) can generate vertical salinity gradients in the upper few meters of the ocean. Vertical stratification can be strong under low wind speed conditions when there is little mixing in the

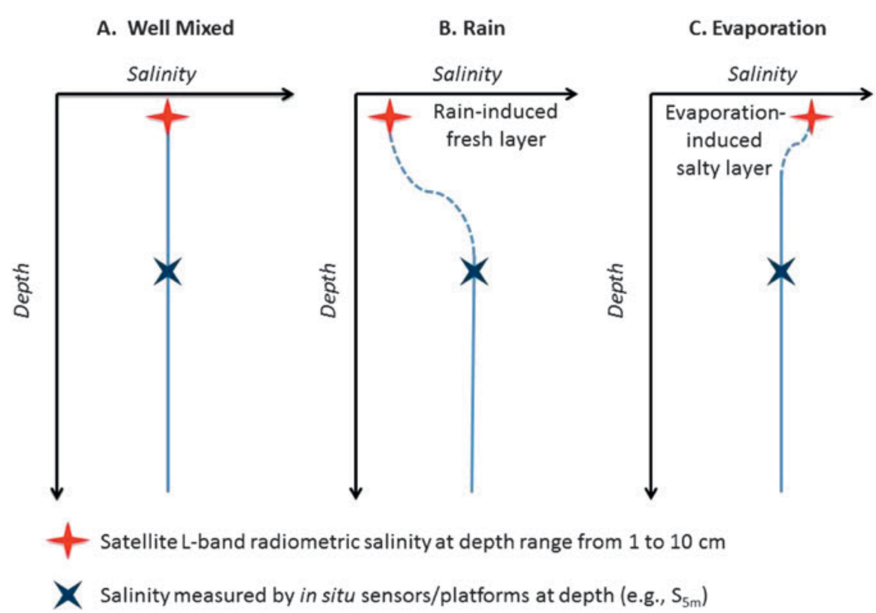

FIG. 2. Schematic diagrams of salinity profiles in the near-surface ocean that are relevant to interpreting satellite and in situ salinity observations. (a) The well-mixed or normal case, where the salinity is uniform as a function of depth. (b) The rain-stratified case, where the freshwater flux causes a stable density stratification to form at the surface and a decrease in salinity with decreasing depth. (c) The evaporation case, where evaporation at the water surface causes an increase in salinity with decreasing depth. Details concerning the formation of the rain and evaporation cases are provided in sections titled "Rain freshening" and "Subfootprint variability."

upper few meters of the ocean. When the wind speed at the ocean surface is greater than ~6 m s^{-1}, wind stress–induced momentum tends to homogenize the upper few meters of the ocean's surface layer (Matthews et al. 2014). When cooling at the surface leads to unstable density stratification, as typically happens at nighttime, convective overturning can also generate a well-mixed surface layer. Regardless of the source of the mixing, salinity is homogeneous throughout the well-mixed layer; this homogeneous condition is considered to be the "normal" case, characterized by a salinity profile that is constant with depth, as shown in Fig. 2a. For the normal condition, radiometrically measured salinity is expected to be comparable to in situ salinity anywhere in the near-surface layer. The sections titled "Rain freshening," "Freshwater plumes," and "Evaporation" discuss the processes that lead to surface freshening (i.e., negative surface salinity anomalies; Fig. 2b) and surface salinification (i.e., positive surface salinity anomalies; Fig. 2c). Based on observational salinity data, the magnitudes of vertical salinity gradients during these conditions will be estimated. These processes, in particular rain freshening and freshwater plumes, are also associated with strong horizontal variability. In the section titled "Subfootprint variability," we discuss subfootprint variability in a wider context.

Rain freshening. Salinity in the upper ocean, especially in the ocean surface boundary layer (OSBL), is subject to large spatial and temporal variability due to various contributing processes, including freshwater influx from precipitation. The scales of this variability, though not well understood or quantified, are assumed to be related to the modification of the freshwater input by the air–sea fluxes of heat and momentum, upper-ocean mixing, and advection. Low-latitude ocean regions characterized by strong rainfall, low to moderate surface winds, and high advection are therefore expected to display relatively strong spatial and temporal variability in SSS.

Under normal conditions when no rainfall is present, the OSBL is characterized by a nearly uniform density, active vertical mixing, and a high rate of turbulence dissipation (Stevens et al. 2011; Sutherland et al. 2014a). As a result, vertical salinity gradients in the upper 10 m are expected to be small (Henocq et al. 2010; Anderson and Riser 2014). In regions where normal conditions dominate, it is appropriate to neglect vertical salinity gradients when using Argo for large-scale validation of SMOS and Aquarius SSS. However, in cases where rainfall induces a near-surface vertical salinity gradient, it is possible that salinity measurements at depths of a few meters might not accurately reflect SSS measured by the satellite in the upper few centimeters. Therefore, Argo measurements made at a few meters depth might not be suitable for validating satellite measurements of SSS.

When averaged globally, rain-induced salinity stratification of the upper mixed layer creates a bias of about −0.02 pss between the salinity measured at a few centimeters and at a few meters. Regional averaging shows that this bias increases to −0.03 pss in the tropics (Drucker and Riser 2014). Rain-induced salinity anomalies and near-surface haloclines resulting from individual rain events were extensively observed in the western Pacific warm pool during the Tropical Ocean and Global Atmosphere (TOGA) Coupled Ocean–Atmosphere Response Experiment (COARE; Soloviev and Lukas 1996, 1997) and in the Bay of Bengal during the Joint Air–Sea Monsoon Interaction Experiment (JASMINE; Webster et al. 2002). More recently, vertical salinity gradients between the upper centimeters and a few meters depth have been observed by Argo surface temperature salinity (STS) profilers (Anderson and Riser 2014), the Air–Sea Interaction Profiler (ASIP; Ward et al. 2014; Walesby et al. 2015a; Sutherland et al. 2014b), the towed Surface Salinity Profiler (SSP; Asher et al. 2014a), shipboard thermosalinographs (TSGs) at two depths (Asher et al. 2014a), and surface drifters (Reverdin et al. 2012).

While near-surface vertical salinity gradients from individual rain-induced freshening events can be large (>1 pss between a few centimeters and a few meters), the distribution of rain events in both space and time is relatively sparse, even in regions characterized by high rainfall. For example, several recent studies have estimated that on average rain-induced surface freshening occurs ~12% of the time when considering the global ocean and ~16% of the time when considering the tropics (Boutin et al. 2013; Anderson and Riser 2014; Drucker and Riser 2014; Meissner et al. 2014). Similarly, Anderson and Riser (2014), using Argo STS float measurements, found that salinity in the upper 4 m is, in most cases, well mixed (i.e., the difference between salinity at a few centimeters and 4 m is less than 0.1 pss for 97% of the observations). Observational studies have consistently shown that, in most cases, near-surface fresh anomalies produced by rainfall are eliminated quickly (typically within a few hours) by mixing, advection, and vertical convection. For example, the deepening of fresh cells to 40-m depth has been observed in the five hours after rainfall with a surface freshening signature of 0.12 pss (Wijesekera et al. 1999; Soloviev et al. 2002).

On the other hand, Walesby et al. (2015a) observed a fresh lens that persisted for more than 15 hours, with little background mixing. The processes governing the vertical and horizontal evolution of fresh lenses are not well understood.

Several studies have attempted to quantify the difference between satellite and in situ salinity to determine the value of the rain freshening effect ΔS (pss) as a function of rainfall rate R (mm h^{-1}) and time since rainfall. Unfortunately, both rain- and wind-generated roughness increase the microwave emissivity of the sea surface, mimicking a decrease in satellite-derived salinity measurements. Consequently, the effect of increased roughness must be addressed before determining the freshening due to rain. Although the effect of wind on roughness (and microwave emissivity) is relatively well known, rain-induced roughness is less understood. The Aquarius instrument is useful for studying this problem because the collocated L-band radiometer and L-band scatterometer are both sensitive to changes in surface roughness, whereas the scatterometer is insensitive to changes in salinity, thereby providing the means for isolating the effects due to surface roughness. Comparison of the signals from the two instruments suggests that the increase in emissivity due to rain-generated roughness is significant at low wind speeds (Tang et al. 2013). At moderate and higher wind speeds, however, rain-generated roughness does not appear to be a major component of the total roughness (Tang et al. 2013; Boutin et al. 2014; Meissner et al. 2014).

Once roughness and atmospheric effects are removed, comparing SSS measured by SMOS (Boutin et al. 2014) or Aquarius (Drucker and Riser 2014; Meissner et al. 2014; Santos-Garcia et al. 2014) to collocated in situ salinities not under the direct influence of instantaneous rainfall shows that $\Delta S/R$ induced by rainfall is estimated to be around -0.15 pss (mm h^{-1})$^{-1}$ (Table 1). However, this bias is an average obtained

Table 1. The range in the rain freshening effect as a function of rain rate ΔS [pss (mm h^{-1})$^{-1}$] as determined by various studies using SMOS and Aquarius data. The rain freshening effect is defined as SSS minus salinity measured at a reference depth of 5 m, and ΔS is calculated as the salinity difference as a function of rain rate.

Satellite[a]	Source for S_{REF}[b]	Data sources	$\Delta S/R$ [pss (mm h^{-1})$^{-1}$]	Range for U[c] (m s^{-1})	Reference
SMOS	Argo SMOS[d]	Tropical Rainfall Measuring Mission (TRMM) Microwave Imager (TMI) AMSR-E Special Sensor Microwave Imager (SSM/I) WindSat	-0.19[e]	3–12	Boutin et al. (2014)
Aquarius	HYCOM Argo	WindSat Special Sensor Microwave Imager/Sounder (SSMIS) F17	-0.17 -0.13 -0.07	0 7 12	Meissner et al. (2014)
Aquarius	Argo	TRMM 3B42	-0.14	—	Drucker and Riser (2014)
Aquarius	HYCOM	Climate Prediction Center (CPC) morphing technique (CMORPH)	-0.20[f] -0.36[g]	—	Santos-Garcia et al. (2014)

[a] Note that neither the SMOS nor the Aquarius salinity retrieval algorithms account for atmospheric attenuation due to liquid cloud water (LCW). It has been estimated that neglecting attenuation by LCW causes an overestimation of ΔS by approximately 10% (Wentz 2005).

[b] S_{REF} is the reference salinity to which satellite measurements are compared.

[c] Term U is wind speed (m s^{-1}); note that not all studies resolved the dependence of ΔS on wind speed.

[d] Boutin et al. (2014) use as S_{REF} either SMOS salinities in rain-free pixels or Argo in rain-free conditions.

[e] Considering various periods and various tropical regions, Boutin et al. (2014) found slopes ranging between -0.16 and -0.22, with an average of -0.19.

[f] Slope obtained in the meridional range 15°N–15°S (Santos-Garcia et al. 2014).

[g] Slope obtained in the meridional range 35°S–35°N (Santos-Garcia et al. 2014).

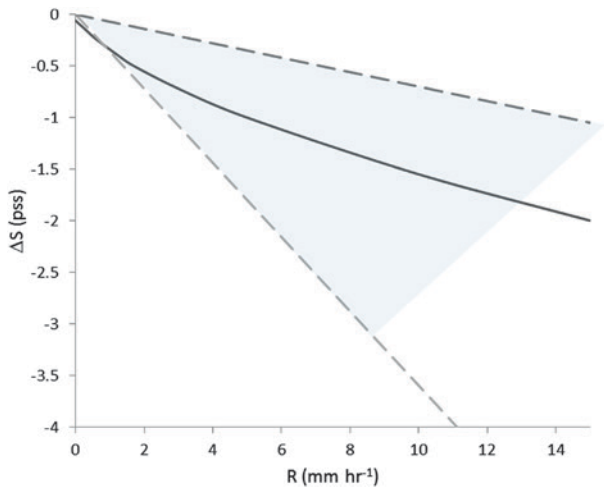

Fig. 3. The rain freshening effect Δ*S* plotted as a function of rain rate *R*. The solid line shows Δ*S* derived from the surface renewal model of Schlüssel et al. (1997). The shaded area shows the range of Δ*S*/*R* relationships derived from satellite SSS studies listed in Table 1. The variability in Δ*S*/*R* relationships is related to wind speed variability as well as to the various satellite salinity, reference salinity, and rain-rate products used in the studies listed in Table 1.

under a range of environmental conditions (wind, rain history, stratification, net heat flux, etc.). Available direct measurements of Δ*S* under different conditions suggest that it is unlikely that DS for a particular rain event can be accurately predicted solely by *R*.

Figure 3 shows the dependence of Δ*S* on *R* for the range of Δ*S*/*R* (Table 1) found from satellite SSS. Also shown is Δ*S* as a function of *R* calculated by Schlüssel et al. (1997) as part of TOGA COARE. Schlüssel et al. (1997) determined this relationship for the salinity difference between the molecular diffusion sublayer (about 50 μm) and the bulk salinity, taking into account the effects of the near-surface mixing induced by raindrops. Despite the variability found in the experimental data, the trends derived from the model and the trends derived from satellite measurements agree well. This convergence of results and theory suggests the value of −0.15 pss (mm h^{-1})$^{-1}$ is relatively robust. However, at present there are no concurrent collocated in situ measurements of *R* and near-surface salinity profiles that include the radiometric sampling depth that can be compared with satellite-derived estimates of Δ*S*.

Although the molecular skin layer modeled by Schlüssel et al. (1997) is much thinner than the radiometric measurement depth used to define Δ*S*, it is reasonable to equate salinity across the two depths and expect the model to provide an estimate of Δ*S*. First, Schlüssel et al. (1997) compared their model results to salinity measured between depths of 2 and 3 cm during several rain events. They found that the magnitude of the measured salinity decrease in the upper few centimeters was consistent with their model predictions for the molecular skin layer. Second, Schlüssel et al. (1997) hypothesized that the very near surface is rapidly homogenized when near-surface mixing caused by the impact of raindrops is taken into account. This idea is consistent with the bubble population measurements made by Ho et al. (2000) that show that during rain events the upper few centimeters of the water surface are well mixed.

Further work is needed to resolve the minimum in situ sampling depth that is required to fully resolve the near-surface salinity profile. Ideally, the profile would sample up to the radiometric penetration depth (i.e., 0.01 m). As noted above, however, the kinetic energy imparted to the water surface by raindrops homogenizes the top few centimeters (Ho et al. 2000), implying that the surface is well mixed at least to the radiometric depth. Therefore, techniques that resolve the top few centimeters should be sufficient. Nevertheless, in highly resolved vertical salinity profiles measured with ASIP during two rain events, gradients larger than 0.1 pss between the sea surface at a few centimeters depth and 30-cm depth have been observed (Ward et al. 2014). ASIP profiles also show that rainfall quickly stratifies the OSBL, inhibiting turbulence. This stratification may lead to strong gradients after the rain has ceased.

Rain-induced surface freshening and the resulting stratification appear to depend nonlinearly on the freshwater input volume, the strength and direction of the surface heat fluxes, and wind-induced mixing. Asher et al. (2014a) developed a one-dimensional diffusion model that fit observed vertical salinity profiles for the top 2 m and direct measurements of *R* to modeled salinity profiles by tuning the turbulent diffusivity coefficient and a scale depth for mixing. This model provided the basis for developing a macroscale Rain Impact Model (RIM) by Santos-Garcia et al. (2014). RIM was developed using Aquarius data and Hybrid Coordinate Ocean Model (HYCOM) output (at ~10-m depth) from the Pacific intertropical convergence zone. It estimates the impact on Aquarius SSS based on rain accumulation over the previous 24 h and time since rainfall. The authors show that the difference between 10-m salinity and salinity measured by Aquarius is not only sensitive to *R* when the satellite is overhead but also to the rain history over the past 25 h, especially when wind speed is low.

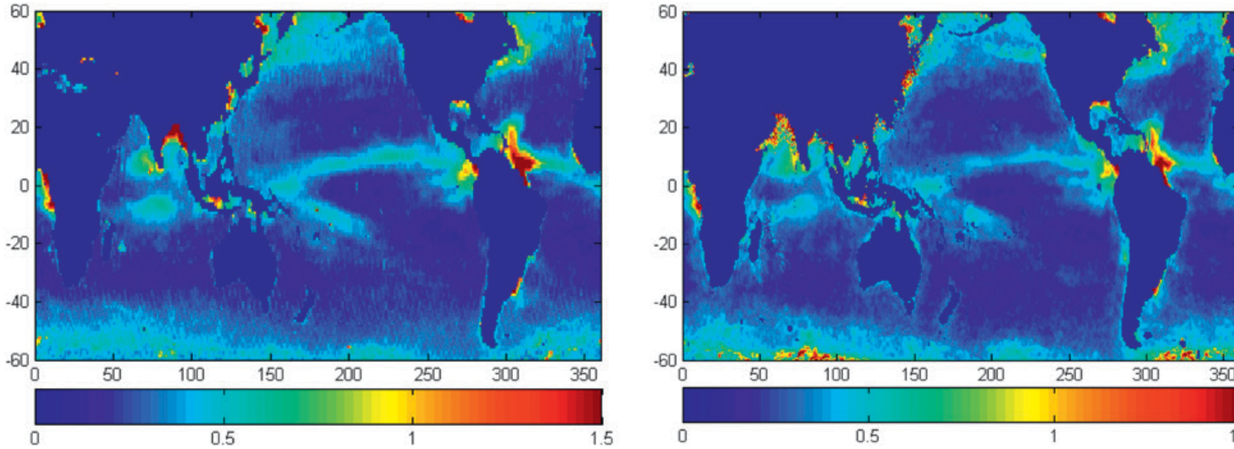

Fig. 4. Standard deviation of SSS as derived from (left) 7-day rolling averages of Aquarius SSS [Combined Active–Passive (CAP) algorithm] and (right) from weekly SMOS data [Centre Aval de Traitement des Données SMOS (CATDS) Expertise Center (CEC) of L'Institut Français de Recherche pour l'Exploitation de la Mer (IFREMER) level 4 product]. Slightly different periods are used to compute these maps: Aug 2011–Dec 2014 for Aquarius and May 2010–Dec 2014 for Aquarius and May 2010–December 2014 for SMOS.

Freshwater plumes. In addition to rain, other sources of freshwater to the surface ocean are river discharge and melting ice. Freshwater plumes from rivers can contribute to the formation and evolution of barrier layers (Sprintall and Tomczak 1992; Pailler et al. 1999; Mignot et al. 2007; Reul et al. 2014b). In situ measurements (e.g., hydrographic ship surveys, Argo floats, voluntary observations from buckets, or TSGs on commercial ships) are too sparse in both space and time to allow full characterization of the generation and evolution of freshwater plumes. Studies have attempted to use ocean color data from the Coastal Zone Color Scanner (CZCS) (Longhurst 1993; Muller-Karger et al. 1995) or the Sea-viewing Wide Field-of-view Sensor (SeaWiFS; Fratantoni and Glickson 2002) to monitor the Amazon River freshwater plume. Reul et al. (2009) demonstrated the first satellite SSS retrieval by using the Advanced Microwave Scanning Radiometer for Earth Observing System (AMSR-E) C-band and X-band channels at 6.9 and 10.7 GHz, respectively, to measure SSS in the Amazon plume. More recently, SMOS and Aquarius data have been used to detect and characterize freshwater plumes for the outflows of the Congo (Hopkins et al. 2013; Reul et al. 2014c; Chao et al. 2015), the Mississippi (Gierach et al. 2013), the La Plata (Guerrero et al. 2014), and the Amazon (Grodsky et al. 2012; Reul et al. 2014b; Fournier et al. 2015; Korosov et al. 2015).

Significant spatial and temporal variability of SSS associated with river plumes can be detected using satellite SSS in regions with large river outflows (Fig. 4). As discussed for rain, near-surface vertical salinity gradients created by freshwater plumes can complicate the comparison of satellite and in situ salinity measurements, as seen with the 2–5 pss m^{-1} difference across the halocline shown by Lentz and Limeburner (1995). Plumes can also cause horizontal salinity gradients with spatial scales smaller than the footprint of the radiometers. Typical horizontal SSS gradients for the plumes from the Amazon (Lentz and Limeburner 1995) or Congo (Chao et al. 2015) exceed 0.2 pss km^{-1} and extend more than 250 km from the river mouth. Therefore, in the vicinity of a river plume, a spatially sparse array of in situ sensors can indicate very different SSS variability than a satellite sensor. High-frequency SSS variations (e.g., tidal effects) can be undersampled by satellite-derived SSS products due to the relatively long revisit time of the satellite (2–3 days for SMOS and 7 days for Aquarius).

At high latitudes, freshwater plumes can be caused by melting sea ice or by meltwater runoff from ice sheets, as has been observed in the seas around Greenland (Straneo and Heimbach 2013). Some of the freshest ocean waters are found in narrow high-latitude coastal currents such as the East Greenland Current. Meltwater from the Antarctic Ice Sheet is the main source of freshwater plumes in the Southern Ocean (Nicholls et al. 2009). While the direct impact of runoff on the coastal currents may be difficult to observe with satellite instruments, model simulations have shown that large meltwater runoff from the Greenland Ice Sheet changes the salinity of the seas surrounding Greenland (Marsh et al. 2010). Although these regions are poorly sampled by in situ observations, SSS retrievals for these areas from satellite L-band radiometers are now routinely available (Brucker et al. 2014a). Unfortunately, the study of freshwater at high latitudes is hindered by the presence of sea ice and icebergs (Brucker et al. 2014b), low water temperature (which reduces the L-band salinity signal-to-noise ratio, thus degrading SSS retrievals), and the prevalence of very rough sea surfaces. Despite these challenges, satellites provide regular monitoring capabilities for SSS that are critically lacking with in situ measurements.

Evaporation. Evaporation can also create vertical salinity gradients in the surface layer and, thereby, potential differences between satellite and in situ salinity measurements (Saunders 1967; Katsaros and Buettner 1969; Soloviev and Lukas 1997; Henocq et al. 2010; Anderson and Riser 2014; Drucker and Riser 2014; Asher et al. 2014b). The nature of the evaporation process and its impact, however, differs from that of precipitation in two major ways. First, evaporation increases salinity and cools the surface waters, both of which serve to increase density. This weakens or destabilizes the density gradient, thereby potentially initiating convective mixing (Yu 2010; Asher et al. 2014b; Soloviev and Lukas 2014). Conversely, precipitation freshens surface waters, reducing density, thereby strengthening the surface stratification and sustaining the freshwater lenses formed by rain (Schlüssel et al. 1997; Henocq et al. 2010; Boutin et al. 2013). Second, evaporation is almost always present, whereas precipitation occurs mostly as episodic events, although the surface freshwater volume flux during rain episodes greatly exceeds the flux due to evaporation over a time period equal to the rain event. During the TOGA COARE field experiments, Lin and Johnson (1996) observed that precipitation rates are highly variable, with peaks of 20 mm day^{-1}, while evaporation rates are more stable, consistently around 3–5 mm day^{-1}. The small volume flux, together with the destabilizing effect on the vertical density profile, implies that evaporation-induced surface salt enrichment (positive salinity anomalies) is relatively weak and short-lived (Yu 2010).

The magnitude of evaporation-induced positive salinity anomalies depends on both evaporation intensity and surface turbulence. Two processes can produce salt increase under evaporation: the salinity skin effect due to near-surface diffusive processes and the daily diurnal cycle in sea surface temperature. Saunders (1967) derived a parameterization for the change of salinity ΔS_{skin} across the salinity skin layer by scaling the layer thickness as the one-third power of the diffusivity. The mutual enhancement between evaporation and wind led him to conclude that the ΔS_{skin} is at most 2%, or around 0.07 pss for a surface salinity of 35 pss, in the extreme condition of low wind speed and large difference in air–sea specific humidity. In support of this result, Fedorov et al. (1979) obtained an estimate of DSskin = 0.12 pss from a laboratory experiment. Yu (2010) produced a global estimate of ΔS_{skin} and suggested a magnitude of 0.05–0.15 pss. Given that the salinity skin layer is typically less than 0.1 mm thick (Zhang and Zhang 2012) and in situ instruments typically measure salinity and temperature deeper than 2 mm below the sea surface (Soloviev and Lukas 2014; Reverdin et al. 2013; Anderson and Riser 2014; Fig. 1), the salinity variations in the skin layer cannot be observed at sea. Nevertheless, Yu (2010) suggested that the salt increment in the skin layer is not a major source of error, because the salty skin layer is usually accompanied by a cooling of 0.2°–0.5°C, which is statically unstable and subject to convective overturn.

Soloviev and Lukas (1997) suggested that continuous evaporation can cause salinity to increase in the diurnal mixed layer, because the positive buoyancy flux due to diurnal heating promotes stable stratification by suppressing turbulent mixing with the water below (see Fig. 5). Confirmation of this hypothesis is provided by several field studies that have documented the existence of a relatively small salt-enriched diurnal cycle that is present under light winds (Soloviev and Lukas 1997; Asher et al. 2014b; Drushka et al. 2014; Hodges and Fratantoni 2014). Asher et al. (2014b) reported that salt-enhanced diurnal surface lenses (0.01–0.05 pss) around 0.5 m thick are common in the subtropical North Atlantic when wind speeds are less than 4 m s^{-1} and the average daily insolation is greater than 300 W m^{-2}. In most cases, however, the magnitude of the salinity increase is usually small, comparable to the uncertainty in the measurements (Soloviev and Lukas 2014; Anderson and Riser 2014). Thus, it is postulated that diurnal salinity anomalies are also unlikely to induce significant biases between radiometrically measured salinities and salinities measured at depths of a few meters (Asher et al. 2014b).

Subfootprint variability. A satellite measurement of SSS represents a near-instantaneous spatial average of the surface salinity field weighted by a function related to the satellite antenna pattern over a characteristic scale that is given by the satellite footprint. If SSS is uniform over the spatial scales averaged by a satellite, then a single in situ salinity measurement anywhere within the satellite footprint provides an accurate ground truth measurement that is representative of the remotely sensed value. However, model simulations (Johannessen et al. 2002) have shown that the salinity field is in some places spatially or temporally inhomogeneous, so that the relationship between the instantaneous, spatially averaged salinity measured by satellite and a single in situ measurement within the satellite footprint is not well understood. In ocean regions characterized by horizontal variability with spatial scales less than the satellite footprint, the subfootprint variability could be a source of difference between satellite and in situ data. When comparing salinity data taken at a point to the spatially averaged value reported by satellite, the SSS variability within the satellite footprint (i.e., subfootprint variability) may need to be taken into consideration.

Commonly used data for purposes of calibrating and validating satellite salinity measurements are those provided by surface drifters, moored buoys in the Tropical Atmosphere Ocean/Triangle Trans-Ocean Buoy Network (TAO/TRITON), or the Prediction and Research Moored Array in the Tropical Atlantic (PIRATA) array, and, most notably, the Argo array (which as of 28 July 2015 contains 3,881 profiling floats and produces the only near-synoptic observations of upper-ocean salinity throughout the World Ocean). However, the approximate 3° × 3° spacing of

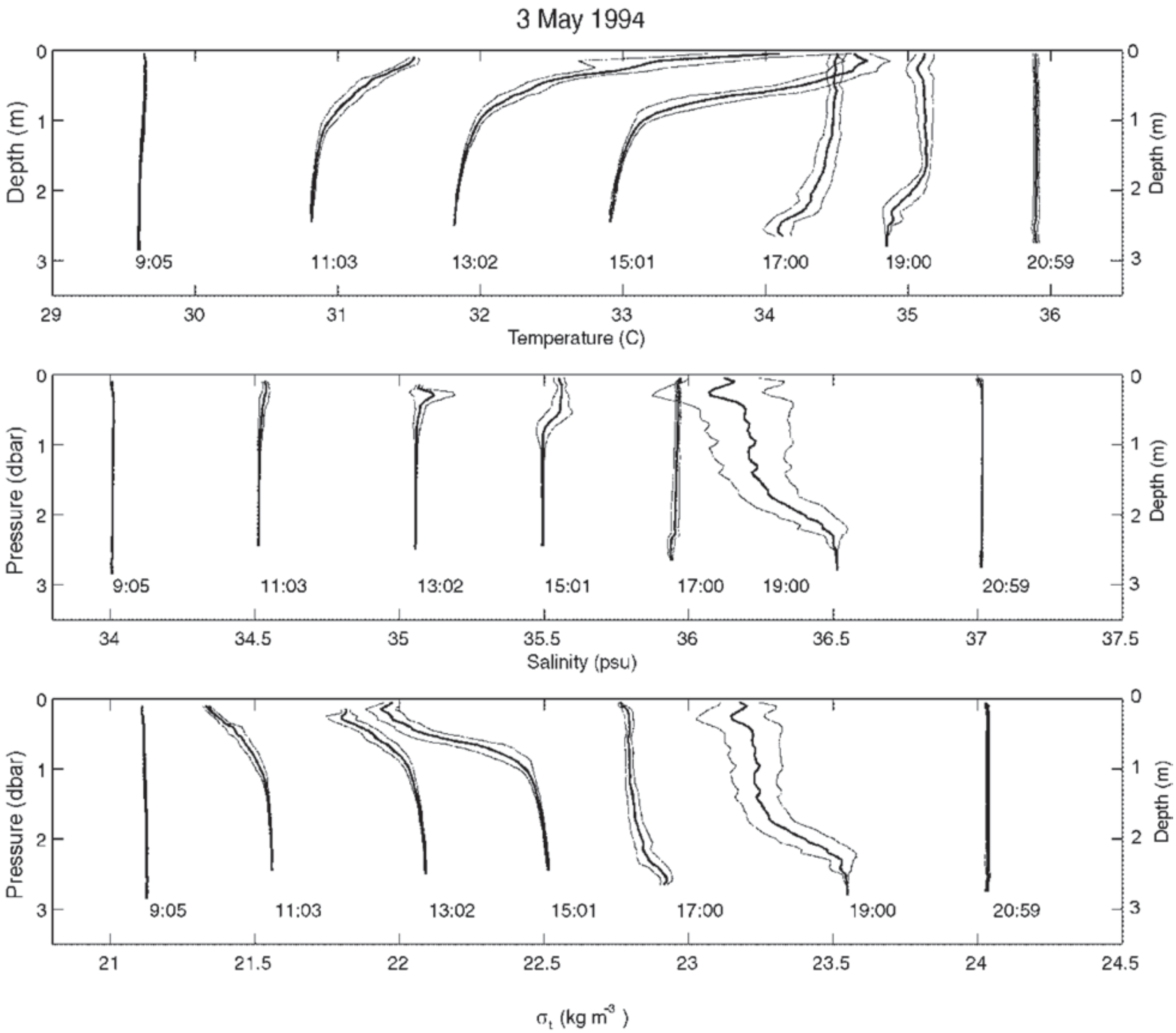

Fig. 5. Vertical profiles of temperature, salinity, and density obtained by averaging ship bow sensor data within 0.1-dbar pressure intervals in 10-min segments. For plotting temporal change, successive temperature, salinity, and density profiles are shifted by 1°C, 0.5 pss, and 0.5 kg m^{-3}, correspondingly. Under each profile the corresponding local solar time is given. The thin lines represent one standard deviation from the mean profiles. Note the excess salinity cumulating in the diurnal mixed layer and diurnal thermocline as a result of evaporation [after Soloviev and Lukas (1997)].

Argo profilers is a factor of 3 larger than the scale of the satellite footprints, which means that Argo does not resolve subfootprint-scale horizontal variability. Similarly, neither TAO/TRITON nor PIRATA can resolve subfootprint-scale variability in SSS.

In contrast to vertical gradients, subfootprint-scale variability in SSS can exist at all wind speeds. Both mesoscale and submesoscale features in the ocean that are responsible for the subfootprint variability of SSS are driven in large part by internal variability associated with ocean circulation. In fact, there can be significant horizontal variability on these larger scales that is not associated with vertical stratification in the upper few meters of the ocean.

Existing observational and modeling studies have provided some understanding of mesoscale and submesoscale SSS variability. For example, in a study comparing in situ data and the output of a high-resolution Massachusetts Institute of Technology (MIT) model of the Atlantic Ocean, Sena Martins et al. (2015) have shown that the annual cycle of SSS explains up to 70% of the total variability observed in some regions of the tropical Atlantic. However, this implies that in most regions at least 30% of variability is on scales other than the seasonal cycle. In fact, Sena Martins et al. (2015) show that SSS variability on time scales shorter than 30 days exceeds 0.1 pss in 42% of the 1° × 1° grid boxes of the model. When the annual cycle is subtracted, the temporal scales of the short-term variability in the model are 4–5 days throughout the Atlantic Ocean (confirmed by results from several mooring stations), and the spatial scales vary between 10 and 150 km. Delcroix et al. (2005) used TSG measurements from the Voluntary Observing Ship (VOS) Program that have 1–3-km resolution, as well as TAO-TRITON and PIRATA moorings at daily resolution, to estimate small-scale SSS variability in the tropical oceans. They reported the mean SSS variability in 2° (longitude) × 1° (latitude) boxes over 10-day intervals to be approximately 0.2 pss. However, there are ocean regions that are characterized by much stronger spatial variability. For example, Maes et al. (2013) analyzed TSG data from the Coral Sea and reported SSS variability as large as 0.6–1 pss over spatial scales of 100 km.

Quality-controlled TSG data (Delcroix et al. 2010; Alory et al. 2015) provide a new, improved resource for estimating subfootprint, near-surface salinity variability (recognizing that TSGs typically sample at 3–7-m depth, depending on the ship, and so do not necessarily represent salinity measured by satellites). Figure 6 shows the analysis of salinity variability derived from the standard deviation within 100-km intervals along a TSG track *s*100km (data produced by Alory et al. 2015; www.legos.obs-mip.fr/observations/sss). The σ100km values were then binned into 2° × 2° grid boxes, and the 95th percentile value σ95 (i.e., the 95% level of the cumulative distribution of σ100km) was computed. Because the distribution of standard deviations within each grid box is not necessarily Gaussian, the average of σ100km in a grid box does not necessarily represent the typical variability. Therefore, σ95 is shown as it represents an upper bound on the variability. Figure 6a provides a map of σ95, and Fig. 6b shows a histogram of σ95, along with the cumulative distributions of σ95 and of 2 × σ100km (which for a Gaussian distribution of σ100km would contain 95% of the points) overlaid. The σ95 histogram (Fig. 6b) shows a median value of 0.12 pss for the ocean regions in Fig. 6a. The cumulative distribution of σ95 is shifted to slightly larger values compared to that of 2 × σ100km because s100km is skewed toward large values (Fig. 6b). However, both cumulative distributions show that in about 25% of the cases SSS spatial variability exceeds 0.15 pss over 100-km scales, and in about 10% of the cases it exceeds 0.25 pss.

Detailed analysis of σ95 regional differences (Fig. 6a) indicates that SSS spatial variability exceeds 0.5 pss in regions affected by western boundary currents, major river plumes (e.g., the Amazon), and several coastal regions, demonstrating that, in many regions, subfootprint-scale SSS variability is larger than 0.1 pss. It should be noted that the instantaneous SSS variability may differ from this map as it was made by combining variability observed during different seasons and years. Finally, patterns of subfootprint variability derived from TSG data agree with the analysis of a HYCOM ocean data assimilation product (which excluded TSG data), conducted by Vinogradova and Ponte (2012). Vinogradova and Ponte (2013) quantified SSS variability within 1° × 1° bins to be as high as 0.2 pss near western boundary currents and in river outflow regions.

EMERGING TECHNOLOGY TO MEASURE NEAR-SURFACE SALINITY. L-band microwave radiometers measure salinity in the top few centimeters of the water column. Development of in situ platforms and instruments that are capable of measuring salinity at these shallow depths is a very active field of research.

On global scales, most near-surface salinity data are from the Argo profiler network. Argo floats measure salinity using a conductivity–temperature–depth (CTD) sensor with a typical uppermost measurement depth of between 3 and 5 m (Boutin and

Martin 2006). This depth is set in order to avoid ingesting sea surface contaminants into the CTD sensor, since these contaminants would degrade sensor stability over the life span of the Argo float.

The STS sensor has recently been developed and implemented on some Argo floats (Anderson and Riser 2014; Riser et al. 2015). An STS-equipped Argo float contains a second, free-flushed, conductivity sensor that is used in conjunction with the standard CTD sensor. The STS sensor samples at 1 Hz concurrently with the standard CTD, both near the float parking depth (980–960 dbar) and again in the upper ocean (20–3 dbar) just before the standard CTD sensor is turned off. After the CTD sensor turns off, the STS sensor continues sampling as the float progresses through the ocean surface, continuing for approximately 500 s as the float prepares to transmit data. Because the STS sensor measures through the film of the ocean surface, its calibration is expected to drift due to fouling. To correct for drift, STS conductivity data are scaled to agree with the mean conductivity from the reference CTD for a region with a small temperature gradient. The resultant mean STS-derived salinity is within 0.01 pss of the reference salinity along the entire profile (Anderson and Riser 2014).

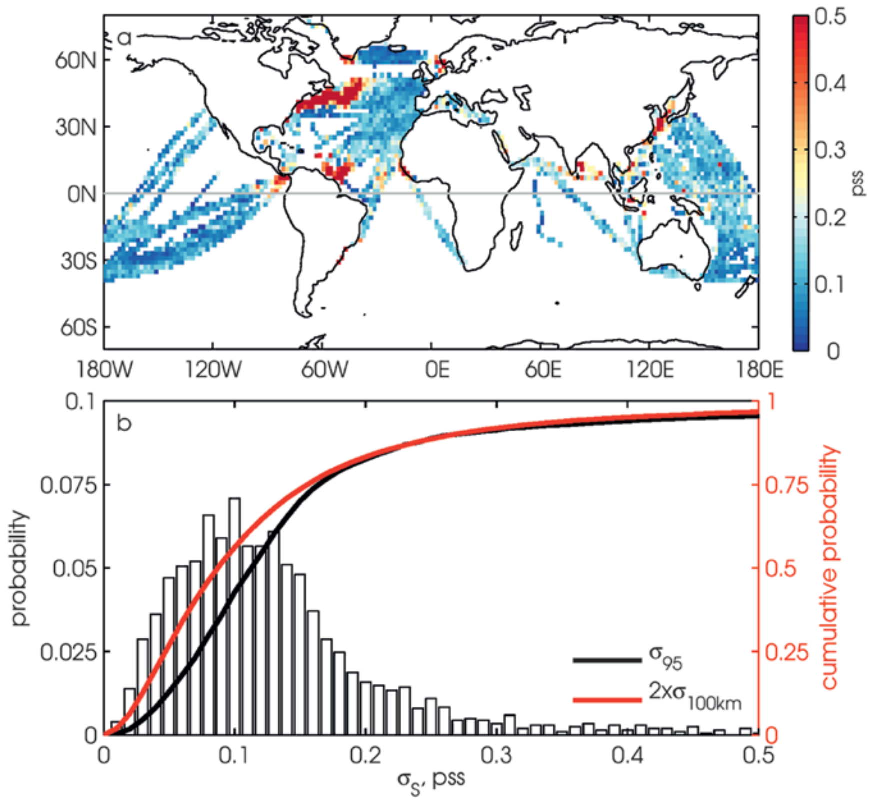

Fig. 6. Analyses of TSG data obtained from the French quality-controlled TSG dataset. (a) The geographical distribution of σ95. (b) The histogram of *s*100km value and cumulative distributions of 2 × σ100km (red line) and σ95 (black line).

During the first Salinity Processes in the Upper Ocean Regional Study (SPURS-1) field experiment (Lindstrom et al. 2015), multiple platforms were deployed and tested, including a mooring with CTD sensors installed at depths of 0.86 and 2.1 m (Farrar et al. 2015); drifters measuring at depths of 0.5 (Centurioni et al. 2015) and 0.2 m (Reverdin et al. 2015); Wave Gliders with CTDs mounted at 0.3 and 8 m (Hodges and Fratantoni 2014); a "salinity snake" that measures salinity in the top few centimeters of the ocean (Schanze et al. 2014; Paulson and Lagerloef 1993); a surface-following towed profiler that measures salinity and temperature at four fixed depths in the upper 2 m of the ocean, with a minimum measurement depth of 0.1 m (Asher et al. 2014a,b); and ASIP, which provides vertical profiles of temperature and salinity in the upper 50 m of the ocean with vertical resolution on the order of a few centimeters and an upper depth of 0.02 m (Fig. 1). Results from the SPURS-1 field experiment are very useful to contrast these different platforms in their abilities to measure the near-surface stratification. For example, in situ platforms measuring at a single point (e.g., ASIP, STS–Argo, and Argo) undersample in terms of area coverage (except in the very special case where two adjacent Argo profilers surface at the same time when a satellite is overhead) and have time scales much longer than the satellite revisit times. Moving instruments (e.g., the Salinity Snake and ship-mounted TSGs) have better spatial coverage, but the data they provide may not be coincident or cotemporaneous with the satellite.

In situ measurement of salinity in the top few centimeters of the ocean is difficult: on nonwave-following platforms, ocean surface vertical motion due to waves advects the water in the desired sampling region past the sensor faster than the response time of most commonly used conductivity-based salinity probes. Even platforms designed to follow large-scale wave motions at the surface have integrated measurement depths of a few centimeters (Fig. 1). Furthermore, conductivity-based salinity estimates are sensitive to the presence of bubbles, and the probes are often sensitive to fouling by biofilms, both of which are prevalent close to the sea surface. Existing methods to measure the near-surface salinity will be improved and new technologies will be developed during future field experiments (e.g., SPURS-2).

SUMMARY AND RECOMMENDATIONS.

The spatiotemporal variability of SSS within a satellite footprint (50–150 km) is a major issue for satellite SSS validation in the vicinity of river plumes, frontal zones, and significant precipitation. In other regions, while much reduced, this variability is often nonnegligible: in 65% of the grid boxes regularly observed by ships of opportunity (Delcroix et al. 2010), the SSS standard deviation along a 100-km transect reaches 0.1 pss. Hence, in many satellite–in situ comparisons, it is of primary importance to account for SSS variability within a satellite footprint. Information on the probability distribution function of SSS in satellite footprints is required, as are autocorrelation statistics such as those determined in some regions by Delcroix et al. (2005). Unfortunately, this variability remains very poorly documented due to the vast undersampling of the majority of the World Ocean (Fig. 6a). Clearly, knowledge of mesoscale and submesoscale SSS variability needs to be improved in terms of magnitude, spatiotemporal distribution, and related dynamics and impacts. In particular, high-resolution in situ measurements must be made in regions of strong variability. Future field campaigns such as SPURS-2 in the eastern tropical Pacific low-salinity region will enhance our understanding of small-scale SSS variability and related dynamical processes in rain-dominated regions.

Although NASA's Soil Moisture Active Passive (SMAP) mission has a primary objective to measure soil moisture, it is possible to use SMAP data to retrieve salinity and improve the spatial sampling of SSS. The upcoming Surface Water and Ocean Topography (SWOT) satellite, to be launched in 2020, will provide sea level (and therefore derived geostrophic current) measurements that will resolve features with a wavelength of 15–100 km, which may facilitate the study of SSS variability on small scales. Emerging high-resolution modeling efforts will also give new insight into the dynamics of mesoscale and submesoscale variability of SSS. Although horizontal salinity variations are more likely to affect comparisons of satellite and in situ salinity, rainfall can in some cases produce vertical salinity gradients exceeding 1 pss m^{-1}; consequently, it is recommended that satellite and in situ SSS measurements less than 3–6 h after rain events should be considered with care when used in satellite calibration/validation analyses. Satellite SSS measurements can be expected to improve in the future, so a detailed understanding of the processes that generate and control the evolution and fate of rain-induced surface freshening events is necessary in order to optimize the use of both satellite and in situ salinity observations. Future studies should, therefore, concentrate on characterizing the vertical salinity profile between the ocean surface and 10-m depth, the penetration of raindrops within the ocean, the effects of splashing and mixing by raindrops, and the small-scale horizontal and vertical advection of freshwater anomalies at the ocean surface. Some Argo profilers enable sampling the upper 3 m of the ocean. Such efforts should be encouraged, including efforts to assess the quality of these new, near-surface measurements. Furthermore, because these processes are coupled to the air–sea fluxes of heat and momentum, it would be advantageous and prudent to perform these assessments under a range of forcing conditions, with particular attention to characterizing necessary ancillary information such as the droplet size spectrum and surface heat fluxes. Ideally, models of salinity stratification in response to precipitation, wind, and advection should reconcile surface and near-surface observations. Parameterizing the near-surface salinity stratification into a global ocean circulation model has been attempted and has shown encouraging results in comparisons with Aquarius SSS and Argo 5–10-m salinity (Moon and Song 2014; Song et al. 2015). Understanding these phenomena at the scales of both an individual rain event and a satellite pixel will help improve the parameterization of rainfall in computational fluid dynamics models.

For the upcoming SPURS-2 field experiment in 2016/17, and looking into the future, new robust salinity sensors are required. For profiling platforms, high spatial resolution is needed. For fixed-depth platforms, better quantification is needed of the actual depth range sampled by the sensor, as well as minimizing platform issues such as flow perturbations and vertical averaging.

ACKNOWLEDGMENTS. This paper was developed from discussions of the Satellite and In Situ Salinity (SISS) mailing list (http://siss.locean-ipsl.upmc.fr) and several

SISS-sponsored working group meetings at the American Geophysical Union (AGU) Fall Meeting and European Geosciences Union (EGU) General Assembly. We thank the following people who read the manuscript and provided comments: Eric Bayler, Rafael J. Catany, Meike Sena Martins, and Yuhe Tony Song.

REFERENCES

Alory, G., C. Maes, T. Delcroix, N. Reul, and S. Illig, 2012: Seasonal dynamics of sea surface salinity off Panama: The far eastern Pacific fresh pool. *J. Geophys. Res.*, **117**, C04028, doi:10.1029/2011JC007802.

——, and Coauthors, 2015: The French contribution to the voluntary observing ships network of sea surface salinity. *Deep-Sea Res.*, **105**, 1–18, doi:10.1016/j.dsr.2015.08.005.

Anderson, J. E., and S. C. Riser, 2014: Near-surface variability of temperature and salinity in the near-tropical ocean: Observations from profiling floats. *J. Geophys. Res. Oceans*, **119**, 7433–7448, doi:10.1002/2014JC010112.

Anguelova, M. D., and P. W. Gaiser, 2011: Skin depth at microwave frequencies of sea foam layers with vertical profile of void fraction. *J. Geophys. Res. Oceans*, **116**, doi:10.1029/2011JC007372.

Asher, W. E., A. T. Jessup, R. Branch, and D. Clark, 2014a: Observations of rain-induced near-surface salinity anomalies. *J. Geophys. Res. Oceans*, **119**, 5483–5500, doi:10.1002/2014JC009954.

——, ——, and D. Clark, 2014b: Stable near-surface ocean salinity stratifications due to evaporation observed during STRASSE. *J. Geophys. Res. Oceans*, **119**, 3219–3233, doi:10.1002/2014JC009808.

Bingham, F. M., G. R. Foltz, and M. J. McPhaden, 2012: Characteristics of the seasonal cycle of surface layer salinity in the global ocean. *Ocean Sci.*, **8**, 915–929, doi:10.5194/os-8-915-2012.

Bourlès, B., and Coauthors, 2008: The PIRATA program: History, accomplishments, and future directions. *Bull. Amer. Meteor. Soc.*, **89**, 1111–1125, doi:10.1175/2008BAMS2462.1.

Boutin, J., and N. Martin, 2006: ARGO upper salinity measurements: Perspectives for L-band radiometers calibration and retrieved sea surface salinity validation. *IEEE Geosci. Remote Sens. Lett.*, **3**, 202–206, doi:10.1109/LGRS.2005.861930.

——, ——, G. Reverdin, X. Yin, and F. Gaillard, 2013: Sea surface freshening inferred from SMOS and ARGO salinity: Impact of rain. *Ocean Sci.*, **9**, 183–192, doi:10.5194/os-9-183-2013.

——, ——, ——, S. Morisset, X. Yin, L. Centurioni, and N. Reul, 2014: Sea surface salinity under rain cells: SMOS satellite and in situ drifters observations. *J. Geophys. Res. Oceans*, **119**, 5533–5545, doi:10.1002/2014JC010070.

Brucker, L., E. P. Dinnat, and L. Koenig, 2014a: Weekly gridded *Aquarius* L-band radiometer/scatterometer observations and salinity retrievals over the polar regions—Part 1: Product description. *Cryosphere*, **8**, 905–913, doi:10.5194/tc-8-905-2014.

——, ——, and ——, 2014b: Weekly gridded *Aquarius* L-band radiometer/scatterometer observations and salinity retrievals over the polar regions—Part 2: Initial product analysis. *Cryosphere*, **8**, 915–930, doi:10.5194/tc-8-915-2014.

Busecke, J., A. L. Gordon, Z. Li, F. M. Bingham, and J. Font, 2014: Subtropical surface layer salinity budget and the role of mesoscale turbulence. *J. Geophys. Res. Oceans*, **119**, 4124–4140, doi:10.1002/2013JC009715.

Centurioni, L. R., V. Hormann, Y. Chao, G. Reverdin, J. Font, and D.-K. Lee, 2015: Sea surface salinity observations with Lagrangian drifters in the tropical North Atlantic during SPURS: Circulation, fluxes, and comparisons with remotely sensed salinity from *Aquarius*. *Oceanography*, **28**, 96–105, doi:10.5670/oceanog.2015.08.

Chao, Y., J. D. Farrara, G. Schumann, K. M. Andreadis, and D. Moller, 2015: Sea surface salinity variability in response to the Congo River discharge. *Cont. Shelf Res.*, **99**, 35–45, doi:10.1016/j.csr.2015.03.005.

Delcroix, T., M. McPhaden, A. Dessier, and Y. Gouriou, 2005: Time and space scales for sea surface salinity in the tropical oceans. *Deep-Sea Res.*, **52**, 787–813, doi:10.1016/j.dsr.2004.11.012.

——, and Coauthors, 2010: Monitoring sea surface salinity in the global ocean from ships of opportunity: The French SSS observation service. *Proceedings of OceanObs'09: Sustained Ocean Observations and Information for Society*, J. Hall, D. E. Harrison, and D. Stammer, Eds., ESA Publ. WPP-306. [Available online at www.oceanobs09.net/proceedings/ac/FCXNL-09A02-1650845-1-ac4a07.pdf.]

Drucker, R., and S. C. Riser, 2014: Validation of *Aquarius* sea surface salinity with Argo: Analysis of error due to depth of measurement and vertical salinity stratification. *J. Geophys. Res. Oceans*, **119**, 4626–4637, doi:10.1002/2014JC010045.

Drushka, K., S. T. Gille, and J. Sprintall, 2014: The diurnal salinity cycle in the tropics. *J. Geophys. Res. Oceans*, **119**, 5874–5890, doi:10.1002/2014JC009924.

Farrar, J. T., and Coauthors, 2015: Salinity and temperature balances at the SPURS central mooring during fall and winter. *Oceanography*, **28**, 56–65, doi:10.5670/oceanog.2015.06.

Fedorov, K. N., V. L. Vlasov, A. K. Ambrosimov, and A. I. Ginsburg, 1979: Investigating the surface layer of evaporating sea water by optical interferometry. *Izv. Akad. Sci. USSR Atmos. Oceanic Phys.*, **15**, 742–747.

Fournier, S., B. Chapron, J. Salisbury, D. Vandemark, and N. Reul, 2015: Comparison of spaceborne measurements of sea surface salinity and colored detrital matter in the Amazon plume. *J. Geophys. Res. Oceans*, **120**, 3177–3192, doi:10.1002/2014JC010109.

Fratantoni, D. M., and D. A. Glickson, 2002: North Brazil Current ring generation and evolution observed with SeaWiFS. *J. Phys. Oceanogr.*, **32**, 1058–1074, doi:10.1175/1520-0485(2002)032<1058:NBCRGA>2.0.CO;2.

Gierach, M. M., J. Vazquez-Cuervo, T. Lee, and V. M. Tsontos, 2013: *Aquarius* and SMOS detect effects of an extreme Mississippi River flooding event in the Gulf of Mexico. *Geophys. Res. Lett.*, **40**, 5188–5193, doi:10.1002/grl.50995.

Grodsky, S. A., and Coauthors, 2012: Haline hurricane wake in the Amazon/Orinoco plume: *AQUARIUS*/SACD and SMOS observations. *Geophys. Res. Lett.*, **39**, L20603, doi:10.1029/2012GL053335.

Guerrero, R. A., and Coauthors, 2014: The salinity signature of the cross-shelf exchanges in the southwestern Atlantic Ocean: Satellite observations. *J. Geophys. Res. Oceans*, **119**, 7794–7810, doi:10.1002/2014JC010113.

Hasson, A., T. Delcroix, and J. Boutin, 2013: Formation and variability of the South Pacific sea surface salinity maximum in recent decades. *J. Geophys. Res. Oceans*, **118**, 5109–5116, doi:10.1002/jgrc.20367.

——, ——, ——, R. Dussin, and J. Ballabrera-Poy, 2014: Analyzing the 2010–2011 La Niña signature in the tropical Pacific sea surface salinity using in situ data, SMOS observations, and a numerical simulation. *J. Geophys. Res. Oceans*, **119**, 3855–3867, doi:10.1002/2013JC009388.

Henocq, C., J. Boutin, G. Reverdin, F. Petitcolin, S. Arnault, and P. Lattes, 2010: Vertical variability of near-surface salinity in the tropics: Consequences for L-band radiometer calibration and validation. *J. Atmos. Oceanic Technol.*, **27**, 192–209, doi:10.1175/2009JTECHO670.1.

Hernandez, O., J. Boutin, N. Kolodziejczyk, G. Reverdin, N. Martin, F. Gaillard, N. Reul, and J. L. Vergely, 2014: SMOS salinity in the subtropical North Atlantic salinity maximum: 1. Comparison with *Aquarius* and in situ salinity. *J. Geophys. Res. Oceans*, **119**, 8878–8896, doi:10.1002/2013JC009610.

Ho, D. T., W. E. Asher, P. Schlosser, L. Bliven, and E. Gordon, 2000: On the mechanisms of rain-induced air-water gas transfer. *J. Geophys. Res.*, **105**, 24 045–24 057, doi:10.1029/1999JC000280.

Hodges, B. A., and D. M. Fratantoni, 2014: AUV observations of the diurnal surface layer in the North Atlantic salinity maximum. *J. Phys. Oceanogr.*, **44**, 1595–1604, doi:10.1175/JPO-D-13-0140.1.

Hopkins, J., M. Lucas, C. Dufau, M. Sutton, J. Stum, O. Lauret, and C. Channelliere, 2013: Detection and variability of the Congo River plume from satellite derived sea surface temperature, salinity, ocean colour and sea level. *Remote Sens. Environ.*, **139**, 365–385, doi:10.1016/j.rse.2013.08.015.

IOC, SCOR, and IAPSO, 2010: The International Thermodynamic Equation of Seawater—2010: Calculation and use of thermodynamic properties. Intergovernmental Oceanographic Commission, Manuals and Guides 56, 220 pp. [Available online at www.teos-10.org/pubs/TEOS-10_Manual.pdf.]

Johannessen, J., and Coauthors, 2002: Scientific requirements and impact of space observations of ocean salinity for modelling and climate studies. ESA Contract 14273/00/NL/DC, NERSC Rep. 214, 272 pp.

Katsaros, K. B., and K. J. Buettner, 1969: Influence of rainfall on temperature and salinity of the ocean surface. *J. Appl. Meteor.*, **8**, 15–18, doi:10.1175/1520-0450(1969)008<0015:IOROTA>2.0.CO;2.

Kerr, Y. H., and Coauthors, 2010: The SMOS mission: New tool for monitoring key elements of the global water cycle. *Proc. IEEE*, **98**, 666–687, doi:10.1109/JPROC.2010.2043032.

Kolodziejczyk, N., O. Hernandez, J. Boutin, and G. Reverdin, 2015: SMOS salinity in the subtropical North Atlantic salinity maximum: 2. Two-dimensional horizontal thermohaline variability. *J. Geophys. Res. Oceans*, **120**, 972–987, doi:10.1002/2014JC010103.

Korosov, A., F. Counillon, and J. A. Johannessen, 2015: Monitoring the spreading of the Amazon freshwater plume by MODIS, SMOS, *Aquarius*, and TOPAZ. *J. Geophys. Res. Oceans*, **120**, 268–283, doi:10.1002/2014JC010155.

Lagerloef, G., 2012: Satellite mission monitors ocean surface salinity. *Eos, Trans. Amer. Geophys. Union*, **93**, 233–234, doi:10.1029/2012EO250001.

Lee, T., G. Lagerloef, H.-Y. Kao, M. J. McPhaden, J. Willis, and M. M. Gierach, 2014: The influence of salinity on tropical Atlantic instability waves. *J. Geophys. Res. Oceans*, **119**, 8375–8394, doi:10.1002/2014JC010100.

Lentz, S. J., and Limeburner, R., 1995: The Amazon River plume during AMASSEDS: Spatial characteristics and salinity variability. *J. Geophys. Res.,* **100**, 2355–2375, doi:10.1029/94JC01411.

Li, Y., W. Han, and T. Lee, 2015: Intraseasonal sea surface salinity variability in the equatorial Indo-Pacific Ocean induced by Madden-Julian oscillations. *J. Geophys. Res. Oceans*, **120**, 2233–2258, doi:10.1002/2014JC010647.

Lin, X., and R. H. Johnson, 1996: Heating, moistening, and rainfall over the western Pacific warm pool during TOGA COARE. *J. Atmos. Sci.*, **53**, 3367–3383, doi:10.1175/1520-0469(1996)053<3367:HMAROT>2.0.CO;2.

Lindstrom, E., F. Bryan, and R. Schmitt, 2015: SPURS: Salinity Processes in the Upper Ocean Regional Study—The North Atlantic Experiment. *Oceanography*, **28**, 14–19, doi:10.5670/oceanog.2015.01.

Longhurst, A., 1993: Seasonal cooling and blooming in tropical oceans. *Deep-Sea Res. I*, **40**, 2145–2165, doi:10.1016/0967-0637(93)90095-K.

Maes, C., and T. J. O'Kane, 2014: Seasonal variations of the upper ocean salinity stratification in the tropics. *J. Geophys. Res. Oceans*, **119**, 1706–1722, doi:10.1002/2013JC009366.

——, B. Dewitte, J. Sudre, V. Garçon, and D. Varillon, 2013: Small-scale features of temperature and salinity surface fields in the Coral Sea. *J. Geophys. Res. Oceans*, **118**, 5426–5438, doi:10.1002/jgrc.20344.

Marsh, R., D. Desbruyeres, J. L. Bamber, B. A. De Cuevas, A. C. Coward, and Y. Aksenov, 2010: Short-term impacts of enhanced Greenland freshwater fluxes in an eddy-permitting ocean model. *Ocean Sci.*, **6**, 749–760, doi:10.5194/os-6-749-2010.

Matthews, A. J., D. B. Baranowski, K. J. Heywood, P. J. Flatau, and S. Schmidtko, 2014: The surface diurnal warm layer in the Indian Ocean during CINDY/DYNAMO. *J. Climate*, **27**, 9101–9122, doi:10.1175/JCLI-D-14-00222.1.

McPhaden, M. J., and Coauthors, 1998: The Tropical Ocean-Global Atmosphere observing system: A decade of progress. *J. Geophys. Res.,* **103**, 14 169–14 240, doi:10.1029/97JC02906.

——, A. J. Busalacchi, and D. L. T. Anderson, 2010: A TOGA retrospective. *Oceanography*, **23**, 86–103, doi:10.5670/oceanog.2010.26.

Mecklenburg, S., and Coauthors, 2012: ESA's soil moisture and ocean salinity mission: Mission performance and operations. *IEEE Trans. Geosci. Remote Sens.*, **50**, 1354–1366, doi:10.1109/TGRS.2012.2187666.

Meissner, T., F. Wentz, J. Scott, and K. Hilburn, 2014: Assessment of rain freshening effects and salinity stratification in the tropics based on the *Aquarius* version 3 salinity product. *Proc. ESA Ocean Salinity Science Workshop*, Exeter, United Kingdom, SMOS+SOS. [Available online at www.smos-sos.org/presentations-ocean-salinity-science-workshop.]

Menezes, V. V., M. L. Vianna, and H. E. Phillips, 2014: *Aquarius* sea surface salinity in the south Indian Ocean: Revealing annual-period planetary waves. *J. Geophys. Res. Oceans*, **119**, 3883–3908, doi:10.1002/2014JC009935.

Mignot, J., C. de Boyer Montégut, A. Lazar, and S. Cravatte, 2007: Control of salinity on the mixed layer depth in the world ocean: 2. Tropical areas. *J. Geophys. Res.*, **112**, C10010, doi:10.1029/2006JC003954.

Minnett, P., and A. Kaiser-Weiss, 2012: Near-surface oceanic temperature gradients. GHRSST Discussion Doc., 7 pp. [Available online at www.ghrsst.org/files/download.php?m=documents&f=120113121306-SSTDefinitionsDiscussion.pdf.]

Moon, J.-H., and Y. T. Song, 2014: Seasonal salinity stratifications in the near-surface layer from *Aquarius*, Argo, and an ocean model: Focusing on the tropical Atlantic/Indian Oceans. *J. Geophys. Res. Oceans*, **119**, 6066–6077, doi:10.1002/2014JC009969.

Muller-Karger, F. E., P. L. Richardson, and D. McGillicuddy. 1995. On the offshore dispersal of the Amazon's Plume in the North Atlantic. *Deep-Sea Res. I*, **42**, 2127–2137.

Nicholls, K. W., S. Østerhus, K. Makinson, T. Gammelsrød, and E. Fahrbach, 2009: Ice-ocean processes over the continental shelf of the southern Weddell Sea, Antarctica: A review. *Rev. Geophys.*, **47**, RG3003, doi:10.1029/2007RG000250.

Pailler, K., B. Bourlès, and Y. Gouriou, 1999: The barrier layer in the western tropical Atlantic Ocean. *Geophys. Res. Lett.*, **26**, 2069–2072, doi:10.1029/1999GL900492.

Paulson, C. A. and G. S. E. Lagerloef, 1993: Fresh surface lenses caused by heavy rain over the Western Pacific Warm Pool during TOGA COARE, EOS Trans. AGU, 74, Suppl. to No. 43, 125.

Qu, T., Y. T. Song, and C. Maes, 2014: Sea surface salinity and barrier layer variability in the equatorial Pacific as seen from *Aquarius* and Argo. *J. Geophys. Res. Oceans*, **119**, 15–29, doi:10.1002/2013JC009375.

Reul, N., S. Saux-Picart, B. Chapron, D. Vandemark, J. Tournadre, and J. Salisbury, 2009: Demonstration of ocean surface salinity microwave measurements from space using AMSR-E data over the Amazon plume. *Geophys. Res. Lett.*, **36**, L13607, doi:10.1029/2009GL038860.

——, B. Chapron, T. Lee, C. Donlon, J. Boutin, and G. Alory, 2014a: Sea surface salinity structure of the meandering Gulf Stream revealed by SMOS sensor. *Geophys. Res. Lett.*, **41**, 3141–3148, doi:10.1002/2014GL059215.

——, Y. Quilfen, B. Chapron, S. Fournier, V. Kudryavtsev, and R. Sabia, 2014b: Multisensor observations of the Amazon-Orinoco river plume interactions with hurricanes. *J. Geophys. Res. Oceans*, **119**, 8271–8295, doi:10.1002/2014JC010107.

——, and Coauthors, 2014c: Sea surface salinity observations from space with the SMOS satellite: A new means to monitor the marine branch of the water cycle. *Surv. Geophys.*, **35**, 681–722, doi:10.1007/s10712-013-9244-0.

Reverdin, G., S. Morisset, J. Boutin, and N. Martin, 2012: Rain-induced variability of near sea-surface T and S from drifter data. *J. Geophys. Res.*, **117**, C02032, doi:10.1029/2011JC007549.

——, and Coauthors, 2013: Surpact: A SMOS surface wave rider for air-sea interaction. *Oceanography*, **26**, 48–57, doi:10.5670/oceanog.2013.04.

——, and Coauthors, 2015: Surface salinity in the North Atlantic subtropical gyre during the STRASSE/SPURS summer 2012 cruise. *Oceanography*, **28**, 114–123, doi:10.5670/oceanog.2015.09.

Riser, S. C., J. Anderson, A. Shcherbina, and E. D'Asaro, 2015: Variability in near-surface salinity from hours to decades in the eastern North Atlantic: The SPURS region. *Oceanography*, **28**, 66–77, doi:10.5670/oceanog.2015.11.

Santos-Garcia, A., M. M. Jacob, W. L. Jones, W. E. Asher, Y. Hejazin, H. Ebrahimi, and M. Rabolli, 2014: Investigation of rain effects on *Aquarius* sea surface salinity measurements. *J. Geophys. Res. Oceans*, **119**, 7605–7624, doi:10.1002/2014JC010137.

Saunders, P., 1967: The temperature at the ocean-air interface. *J. Atmos. Sci.*, **24**, 269–273, doi:10.1175/1520-0469(1967)024<0269:TTATOA>2.0.CO;2.

Schanze, J. J., G. Lagerloef, R. W. Schmitt, and B. A. Hodges, 2014: Snakes on a ship: Surface salinity observations during SPURS. *Extended Abstracts, 2014 Ocean Sciences Meeting*, Honolulu, HI, ASLO-AGU, 073. [Available online at www.sgmeet.com/osm2014/viewabstract.asp?AbstractID=17211.]

Schlüssel, P., A. Soloviev, and W. Emery, 1997: Cool and freshwater skin of the ocean during rainfall. *Bound.-Layer Meteor.*, **82**, 439–474, doi:10.1023/A:1000225700380.

Sena Martins, M., N. Serra, and D. Stammer, 2015: Spatial and temporal scales of sea surface salinity variability in the Atlantic Ocean. *J. Geophys. Res. Oceans*, **120**, 4306–4323, doi:10.1002/2014JC010649.

Soloviev, A., and R. Lukas, 1996: Observation of spatial variability of diurnal thermocline and rain-formed halocline in the western Pacific warm pool. *J. Phys. Oceanogr.*, **26**, 2529–2538, doi:10.1175/1520-0485(1996)026<2529:OOSVOD>2.0.CO;2.

——, and ——, 1997: Observation of large diurnal warming events in the near-surface layer of the western equatorial Pacific warm pool. *Deep-Sea Res. I*, **44**, 1055–1076, doi:10.1016/S0967-0637(96)00124-0.

——, and ——, 2014: *The Near-Surface Layer of the Ocean: Structure, Dynamics, and Applications*. 2nd ed. Springer, 552 pp.

——, ——, and H. Matsuura, 2002: Sharp frontal interfaces in the near-surface layer of the tropical ocean. *J. Mar. Syst.*, **37**, 47–68, doi:10.1016/S0924-7963(02)00195-1.

Song, Y. T., T. Lee, J.-H. Moon, T. Qu, and S. Yueh, 2015: Modeling skin-layer salinity with an extended surface-salinity layer. *J. Geophys. Res. Oceans*, **120**, 1079–1095, doi:10.1002/2014JC010346.

Sprintall, J., and M. Tomczak, 1992: Evidence of the barrier layer in the surface layer of the tropics. *J. Geophys. Res.*, **97**, 7305–7316, doi:10.1029/92JC00407.

Stevens, C., B. Ward, C. Law, and M. Walkington, 2011: Surface layer mixing during the SAGE ocean fertilization experiment. *Deep-Sea Res. II*, **58**, 776–785, doi:10.1016/j.dsr2.2010.10.017.

Straneo, F., and P. Heimbach, 2013: North Atlantic warming and the retreat of Greenland's outlet glaciers. *Nature*, **504**, 36–43, doi:10.1038/nature12854.

Sutherland, G., K. H. Christensen, and B. Ward, 2014a: Evaluating Langmuir turbulence parameterizations in the ocean surface boundary layer. *J. Geophys. Res. Oceans*, **119**, 1899–1910, doi:10.1002/2013JC009537.

——, G. Reverdin, L. Mari, and B. Ward, 2014b: Mixed and mixing layer depths in the ocean surface boundary layer under conditions of diurnal stratification. *Geophys. Res. Lett.*, **41**, 8469–8476, doi:10.1002/2014GL061939.

Swift, C. T., 1980: Passive microwave remote sensing of the ocean—A review. *Bound.-Layer Meteor.*, **18**, 25–54, doi:10.1007/BF00117909.

Tang, W., S. Yueh, A. Fore, G. Neumann, A. Hayashi, and G. Lagerloef, 2013: The rain effect on *Aquarius*' L-band sea surface brightness temperature and radar backscatter. *Remote Sens. Environ.*, **137**, 147–157, doi:10.1016/j.rse.2013.06.016.

Vinogradova, N. T., and R. M. Ponte, 2012: Assessing temporal aliasing in satellite-based surface salinity measurements. *J. Atmos. Oceanic Technol.*, **29**, 1391–1400, doi:10.1175/JTECH-D-11-00055.1.

——, and ——, 2013: Small-scale variability in sea surface salinity and implications for satellite-derived measurements. *J. Atmos. Oceanic Technol.*, **30**, 2689–2694, doi:10.1175/JTECH-D-13-00110.1.

Walesby, K., J. Vialard, P. J. Minnett, A. H. Callaghan, and B. Ward, 2015a: Observations indicative of rain-induced double diffusion in the ocean surface boundary layer. *Geophys. Res. Lett.*, **42**, 3963–3972, doi:10.1002/2015GL063506.

Ward, B., T. Fristedt, A. H. Callaghan, G. Sutherland, X. Sanchez, J. Vialard, and A. Doeschate, 2014: The Air–Sea Interaction Profiler (ASIP): An autonomous upwardly rising profiler for microstructure measurements in the upper ocean. *J. Atmos. Oceanic Technol.*, **31**, 2246–2267, doi:10.1175/JTECH-D-14-00010.1.

Webster, P. J., and Coauthors, 2002: The JASMINE pilot study. *Bull. Amer. Meteor. Soc.*, **83**, 1603–1630, doi:10.1175/BAMS-83-11-1603.

Wentz, F., 2005: The effects of clouds and rain on the *Aquarius* salinity retrieval. Algorithm Theoretical Basis Doc., RSS Tech. Memo. 3031805, 14 pp. [Available online at www.remss.com/papers/aquarius/rain_effect_on_salinity.pdf.]

Wijesekera, H. W., C. A. Paulson, and A. Huyer, 1999: The effect of rainfall on the surface layer during a westerly wind burst in the western equatorial Pacific. *J. Phys. Oceanogr.*, **29**, 612–632, doi:10.1175/1520-0485(1999)029<0612:TEOROT>2.0.CO;2.

Yu, L., 2010: On sea surface salinity skin effect induced by evaporation and implications for remote sensing of ocean salinity. *J. Phys. Oceanogr.*, **40**, 85–102, doi:10.1175/2009JPO4168.1.

Zhang, Y., and X. Zhang, 2012: Ocean haline skin layer and turbulent surface convections. *J. Geophys. Res.*, **117**, C04017, doi:10.1029/2011JC007464.